Simultaneous decoding of cardiovascular and respiratory functional changes from pig intraneural vagus nerve signals

Fabio Vallone[1],*, Matteo Maria Ottaviani[1,2],*, Francesca Dedola[1], Annarita Cutrone[1], Simone Romeni[3], Adele Macrí Panarese[1], Fabio Bernini[2], Marina Cracchiolo[1], Khatia Gabisonia[2,4], Nikoloz Gorgodze[2,4], Alberto Mazzoni[1], Fabio A. Recchia[2,4,5] , Silvestro Micera[1,3]

[1]The BioRobotics Institute and Department of Excellence in Robotics and Artificial Intelligence, Scuola Superiore Sant'Anna, Pisa, Italy.

[2] Institute of Life Sciences, Scuola Superiore Sant'Anna, Pisa, Italy.

[3]Bertarelli Foundation Chair in Translational Neural Engineering, Center for Neuroprosthetics and Institute of Bioengineering, Ecole Polytechnique Federale de Lausanne, Lausanne, Switzerland.

[4]Fondazione Toscana Gabriele Monasterio, Pisa, Italy.

[5]Department of Physiology, Cardiovascular Research Center, Lewis Katz School of Medicine at Temple University, Philadelphia, Pennsylvania, USA.

(*equal contribution)

Corresponding authors: Silvestro Micera (silvestro.micera@santannapisa.it[epfl.ch]) and Fabio Recchia (fabio.recchia@santannapisa.it).

Abstract

Bioelectronic medicine is opening new perspectives for the treatment of some major chronic diseases through the physical modulation of autonomic nervous system activity. Being the main peripheral route for electrical signals between central nervous system and visceral organs, the vagus nerve (VN) is one of the most promising targets. Closed-loop neuromodulation would be crucial to increase effectiveness and reduce side effects, but it depends on the possibility of extracting useful physiological information from VN electrical activity, which is currently very limited.

Here, we present a new decoding algorithm properly detecting different functional changes from VN signals. They were recorded using intraneural electrodes in anaesthetized pigs during cardiovascular and respiratory challenges mimicking increases in arterial blood pressure, tidal volume and respiratory rate. A novel decoding algorithm was developed combining discrete wavelet transformation, principal component analysis, and ensemble learning made of classification trees. It robustly achieved high accuracy levels in identifying different functional changes and discriminating among them. We also introduced a new index for the characterization of recording and decoding performance of neural interfaces. Finally, by combining an anatomically validated hybrid neural model and discrimination analysis, we provided new evidence suggesting a functional topographical organization of VN fascicles. This study represents an important step towards the comprehension of VN signaling, paving the way to the development of effective closed-loop bioelectronic systems.

Keywords

Introduction

The autonomic nervous system (ANS) plays a crucial role in the self-governed maintenance of body homeostasis. In ANS peripheral nerves, afferent and efferent fibres run together, providing bidirectional communication between specific circuits of the central nervous system and visceral organs. The artificial modulation of this complex circuitry is the challenging goal of bioelectronic medicine (BM), a highly promising alternative to some limited pharmacological tretments[1–3]. Among the main ANS nerves, the vagus nerve (VN) represents a privileged target as it modulates vital functions like respiration, circulation and the digestion[4]. VN stimulation (VNS) of cervical segments has shown a great potential for the treatment of a wide range of pathological conditions such as epilepsy[5], chronic heart failure[6], and inflammatory diseases[7,8]. However, the formidable amount of afferent and efferent signals that simultaneously cross this VN segment, the numerous VNS side-effects[9] and the discovery of VN involvement in the regulation of complex functions like immunity[10] or central neuroplasticity[11,12] highlight the need for high precision and selectivity. In an ideal scenario, the therapeutic stimulation or inhibition of VN or any other ANS nerve should be: a) selectively directed to specific efferent or afferent fibres and b) regulated by a closed-loop feedback, thus adapting the stimulation to patient-specific conditions[13–16]. Importantly, the co-existence of afferent and efferent signals in the VN points to the possibility that the feedback loop is originated and closed at the same anatomical site. Nonetheless, VNS is currently applied in an open-loop fashion[17,18] and mainly delivered using epineural cuff-like electrodes, because of their relatively low invasiveness and versatility for chronic applications[19,20].

69 The first step for the development of a closed loop modality would be the precise

70 identification of physiological "states" by processing the autonomic neural signals. Different

71 strategies have been recently adopted to extract function-specific markers from neural

72 activity using epineural electrodes[3,21–25]. Specific neurograms related to the respiratory

73 cycle[21,22] and blood pressure fluctuations[3] were recorded from pig VN using bipolar/tripolar

74 ring cuff electrodes, while decoding strategies and methodological frameworks led to the

75 identification of cytokine- and hypoglycemia/hyperglycemia-specific neural activity markers

76 in murine VN and carotid sinus nerve[23-25]. However, epineural electrodes display a limited

77 selectivity and can only record the compound activity that provides a global picture of neural

78 signal trafficking[26–28]. Therefore, intraneural electrodes have been developed and

79 successfully employed by us and others to enhance selectivity and increase the signal-to-

80 noise ratio of recordings[26,29] in somatic nerves[13,16,30,31]. Nevertheless, this technology has

81 received very limited attention for VN applications and only one preliminary study has been

82 published to date[32], which was based on a simple experimental protocol (steady neural

83 activity) and a limited signal recording capacity (i.e. 4-channel electrode longitudinally

84 implanted).

85 Here, we performed the first comprehensive study testing intraneural VN recording to

86 identify physiological (arterial and respiratory) changes. To this aim, we recorded VN activity

87 through intraneural multi-channel electrodes in anaesthetized pigs at baseline and during

88 alterations in blood pressure and respiratory parameters, collectively named "functional

89 challenges". To discriminate between baseline condition and functional challenges and to

90 investigate a possible functional organization of VN fascicles, we developed novel decoding

91 algorithms and hybrid modeling framework (see next section and Methods).

Results

Experimental setup and decoding method to classify functional challenges against baseline

To study the feasibility of decoding relevant physiological states based on VN neural activity, intrafascicular multichannel electrodes[40] were implanted into the cervical VN of 4 anaesthetized and artificially ventilated pigs (p1, ..., p4) (Fig.1 a,b). Neural activity was recorded at baseline and during functional challenges obtained by infusing the vasopressor angiotensin II (AngII) to increase baseline blood pressure (BP) by 150% and/or by varying the ventilator parameters to increase respiratory rate (RR) and/or tidal volume (TV). These 3 functional challenges, named BPC, RRC and TVC, were compared to baseline condition and among them (Fig.1c and Methods for details). To obtain the desired vasopressor effect, AngII infusion was maintained for 8.8 ± 0.8 min (n=5) and mean BP increased from 76 ± 2.2 mmHg up to 110 ± 2.6 mmHg (n=5).

A decoding algorithm was developed to process multivariate signals acquired from the multi-channel intraneural electrodes. To extract from the neural activity relevant features encoding for the functional challenges, we first employed a multi-scale decomposition analysis based on the discrete wavelet transform[33,34] to extract the high frequency component (>1500 Hz) of our recordings. Subsequently, we focused on the direction of greatest variance by using principal components analysis[35] (Fig. 1d and Methods for details). Then, an ensemble of classifiers made on classification trees[36,37] was trained and we assessed the classification performance on the test set using accuracy values (Fig. 1e and Methods for details).
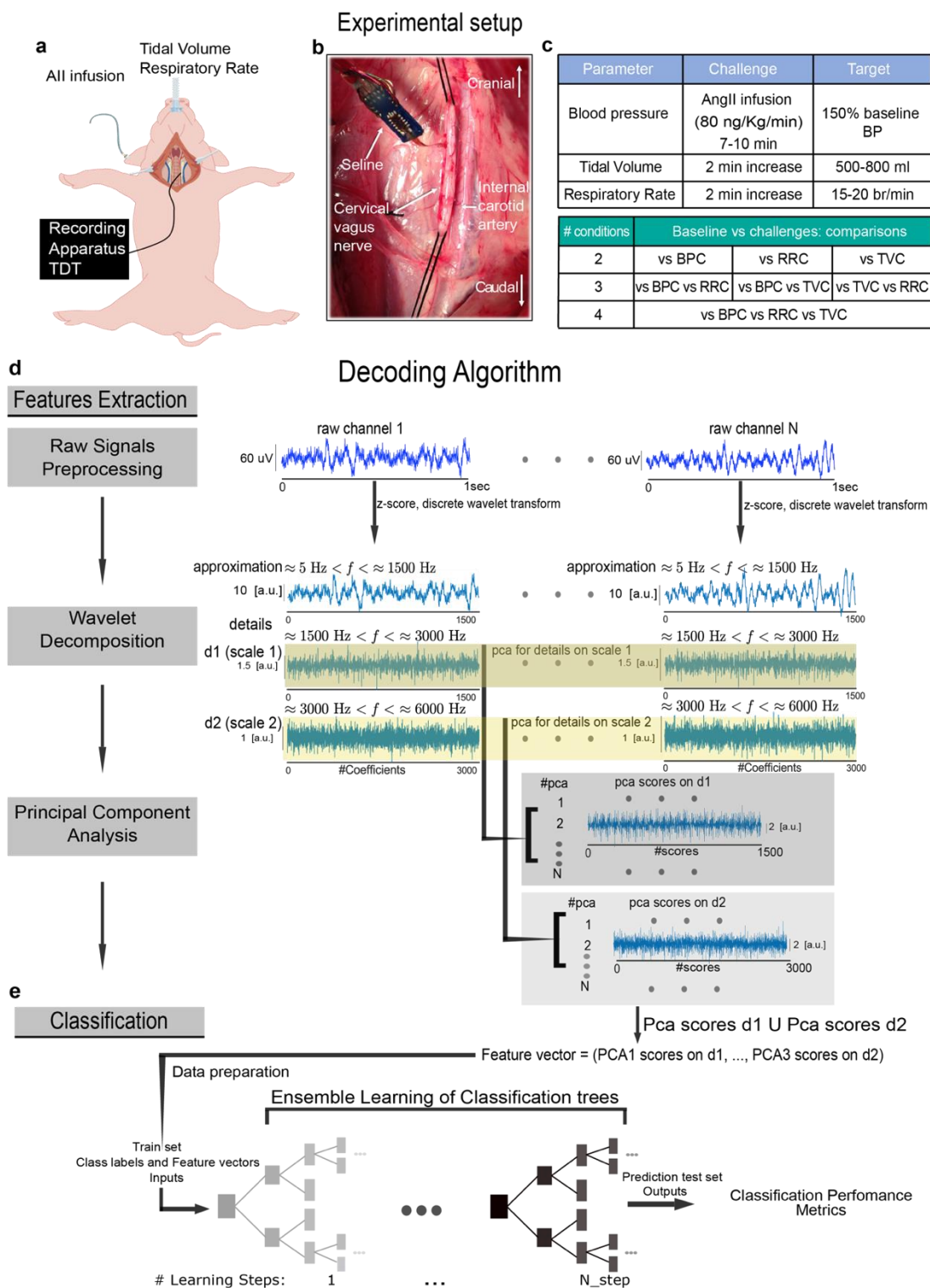
Fig. 1 Schematic representation of the experimental setup and decoding algorithm **a,b** Recording apparatus and electrode implantation **c** Summary of the in vivo protocol and comparisons . **d** Decoding algorithm. Feature extraction was performed on raw signals by applying principal component analysis on wavelet details relative to two different scales. **e** Decoding performed with ensemble learning based on classification tree combined with random undersampling and boosting procedure (see Methods) was applied on feature vectors. Decoding performance was assessed by means of confusion matrices and accuracy level.

121 We tested our decoding algorithm in different scenarios, i.e., considering a progressively

122 larger number and type of functional challenges. In two pigs (p3 and p4) we also studied the

123 variation of the decoding performances relative to the positioning of two SELINEs (s1, s2)

124 and (s3, s4) within the same nerves, thus testing the following combinations: p3-s1, p3-s2

125 and p4-s3, p4-s4.

126

127 **Decoding the response to a single functional challenge**

128 We started with the simplest case in which we sought to discriminate only one of the three

129 functional challenges against baseline. For baseline vs BPC, we achieved a mean accuracy

130 level over the different recordings equal to 90.7$\pm$5.7% as shown in Fig. 2a (n=5, see

131 Supplementary Fig. 1a for confusion matrices).

132 High-level accuracy during increased RRC was also obtained, equal to 89.1$\pm$3.9%, as

133 shown in Fig. 2b (n=4, see also Supplementary Fig. 1b for confusion matrices).

134 Measurements during TVC yielded more heterogeneous results compared to the other

135 challenges. In pig p2 that was implanted with TIME t2 (p2-t2), we achieved high accuracy

136 level equal to 83.5% ([75.8%, 89.5%], Confidence Interval p=0.05, see Fig. 2c and

137 Supplementary Fig. 1c for confusion matrices).

138 Moreover, the decoding accuracy during TVC was strongly dependent on the electrode

139 positioning. In fact, in animals implanted with s1 and s4, i.e. p3-s1 and p4-s4, we obtained

140 accuracy values statistically not different from chance level (p>0.05, binomial test, see Fig.

141 2c and Supplementary Fig. 1c for confusion matrices), i.e. 45.7% for p3-s1 ([36.8%, 54.7%],

142 Confidence Interval p=0.05) and 52.3% for p4-s4 ([43.3%, 61.2%], Confidence Interval

143 p=0.05). In the same animals, but with different electrode positioning, we achieved a high

144 level of accuracy of 95.5% for p3-s2 ([90.5%, 98.31%], Confidence Interval p=0.05) and

145 75% for p4-s3 ([66.6%, 82.2%], Confidence Interval p=0.05, see Fig. 2c and Supplementary

146 Fig. 1c for confusion matrices). Interestingly, in this scenario TIMEs and SELINEs performed

147 similarly. Indeed, if we consider only the maximum accuracies achieved in each animal, thus

148 neglecting possible confounding effects of electrode positioning, the TIME t1 in p2 achieved

149 the maximum accuracy across animals in the case of baseline vs. BPC (Fig 2a), while

150 SELINE s2 implanted in p3 performed better in the baseline vs. TVC, achieving a maximum

151 accuracy in the animal p3-s2 (Fig. 2c). No significant differences between maximum

152 accuracies were found for baseline vs. RRC (see Fig. 2b, p2-t2 vs. p4-s3 and p2-t2 vs p3-

153 s2, p>0.05 Chi square test, Bonferroni correction).

154 The differences between two levels of RRC and TVC in p2 (from 10 to 15 respiratory

155 cycles/min and from 400 to 500 ml, respectively) compared to p3 and p4 (from 10 to 20

156 respiratory cycles/min and from 400 to 800 ml, respectively) did not indicate strong

157 differences in the decoding performances. In fact, if we compared the maximum accuracies

158 obtained in a single animal (i.e., to neglect the effect of a possible dependency of electrode

159 position) only in the case of baseline vs. TVC, the accuracy achieved in p2-t2 was lower

160 than the maximum one observed in p3-s2 (Fig.2c ,p<0.05 Chi square test, Bonferroni

161 correction), while no statistical differences were found (p>0.05 Chi square test, Bonferroni

162 correction) in the other cases (Fig.2b p2-t2 vs p3-s4, p2-t2 vs p4-s3, and Fig.2c p2-t2 vs

163 p4-s3).

164 Finally, a dependence on electrode position was also observed in pigs p4 and p3 for the

165 comparisons of baseline vs. BPC (Fig.2a) and baseline vs. RRC (Fig. 2c), respectively. In

166 fact, the accuracy value for p4-s3 (96%, [92.5%, 98.1%] Confidence Interval p=0.05, Fig.2a)

167 was greater than p4-s4 (68.5%, [62.2%, 74.3%] Confidence Interval p=0.05, Fig.2a)

168 (p<0.001 Chi square test, Bonferroni correction). Moreover, in pig p3 implanted with SELINE

169 s1 and s2, i.e. p3-s1 and p3-s2, we achieved a lower level of accuracy for p3-s1 (74%,

170 [66.1%, 80.9%] Confidence Interval p=0.05, Fig.2b) with respect to p3-s2 (93.2%, [87.5%,

171 96.8%] Confidence Interval p=0.05, Fig.2b) (p<0.001 Chi square test, Bonferroni

172 correction).

173
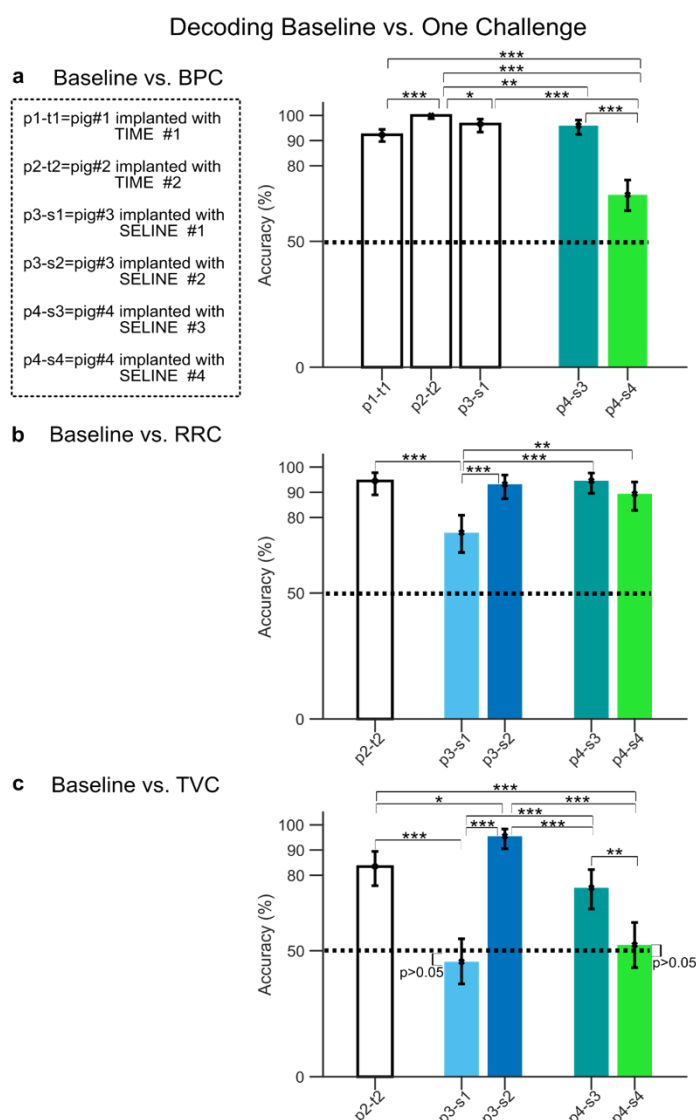
Fig. 2 Decoding accuracy for baseline condition vs. a single functional challenge **a,b,c** Accuracy level together with p=0.05 confidence interval (error bars, Clopper-Pearson method) for the comparison between baseline and BPC (panel a), RRC (panel b) and TVC (panel c). For all panels, colored bars indicate the same animal implanted with two different electrodes. Dashed lines represent chance level. To test statistically significant differences with respect to chance level in the cases where confidence intervals overlapped with chance level, a binomial test was used (panel c, animals p3-s1 and p4-s3, p>0.05 binomial test). Statistical comparisons between animals were assessed by using a Chi square test Bonferroni corrected for multiple comparisons (*p<0.05, **p<0.01, ***p<0.001).

182

Decoding the response to multiple functional challenges

184 We increased the complexity of the decoding task by producing two simultaneous functional

185 challenges in different physiological systems, e.g. BPC plus RRC or TVC, or in the same

186 system, namely RRC and TVC. As expected, the highest accuracy levels were achieved

187 when alterations were simultaneously induced in different systems (Fig. 3a,b and

188 Supplementary Fig. 2a,b).

189 The accuracy values for the BPC vs. RRC case were 81.6±7.1% (n=4), as shown in Fig. 3a

190 and Supplementary Fig. 2a for confusion matrices. Statistical differences between accuracy

191 values of p4-s3 (81.7%, [76.7%, 86.1%] Confidence Interval p=0.05) and p4-s4 (81.7%,

192 [57.1%, 68.8%] Confidence Interval p=0.05) indicate dependency on electrode position

193 (p<0.001 Chi square test, Bonferroni corrected).

194 Dependency on electrode position was observed also for BPC vs TVC: in the animal

195 implanted with s4, i.e. p4-s4, we found a statistically significant different accuracy level

196 (54.2%, [48.1%, 60.2%] Confidence Interval p=0.05), than for p4-s3 (83.9%, [78.8%, 88.1%]

197 Confidence Interval p=0.05) (p<0.001 Chi square test, Bonferroni corrected, see Fig. 3b).

198 Overall, we obtained a mean over recordings 75.8±8.2% accuracy (n=4), as shown in Fig.

199 3b and Supplementary Fig. 2b for confusion matrices.

200 We were also able to reliably decode the two respiratory challenges RRC and TVC when

201 occurring simultaneously. We found that in animals p3 and p4 the electrodes s2 and s3

202 achieved a high level of accuracy, 85.6% ([79.4%, 90.4%] Confidence Interval p=0.05) and

203 81% ([74.6%,86.4%] Confidence Interval p=0.05), respectively, as shown in Fig. 3c and

204 Supplementary Fig. 2c. In contrast, in the same animals, the electrodes s1 and s4 implanted

205 in different positions were only able to reach accuracy values equal to 44.8%([37.5%, 52.3%]

206 Confidence Interval p=0.05) and 45%([37.2%, 52.8%] Confidence Interval p=0.05) for p3-s1

207 and p4-s4, respectively, as shown in Fig. 3c and Supplementary Fig. 2c. Moreover, in p1

208 implanted with TIME t2, we achieved accuracy values equal to 68.9% ([61.2%, 75.9%]

209 Confidence Interval p=0.05). In this configuration, TIMEs seemed to perform better than

210 SELINE in two cases, as the maximum accuracy for the cases BPC vs. RRC and BPC vs.

211 TVC were obtained by p2-t2 (Fig. 3a,b, p2-t2 vs p3-s1and p2-t2 vs. p4-s3, p<0.001 Chi

212 square test, Bonferroni correction, respectively). However, the maximum accuracy for TVC

213 vs. RRC was obtained by SELINE s2 implanted in p3, i.e. p3-s2 (Fig. 3c, p3-s2 vs p2-t2,

214 p<0.01 Chi square test, Bonferroni correction).

215 Finally, we studied the most complex scenario of our experimental dataset in which all types

216 of functional challenges (one cardiovascular and two respiratory) are decoded

217 simultaneously. As discussed above, also in this case we found that decoding performances

218 depended on electrode positioning within the same animal p4. The accuracy levels were

219 73.7% for p4-s3 ([68.5%, 78.5%] Confidence Interval p=0.05) and 45.3% for p4-s4 ([39.7%,

220 51%] Confidence Interval p=0.05), as shown in Fig. 4a and Fig4c for confusion matrices.

221 The highest accuracy among animals was obtained by TIME t2 implanted in p2, i.e. p2-t2,

222 with a value equal to 87.3% ([83.3%, 90.6%] Confidence Interval p=0.05) (Fig 4a).

223 Furthermore, to better understand why different accuracy values were obtained in our

224 datasets, we searched for a possible correlation between the electrode discrimination ability,

225 i.e. the sensitivity of the recording sites to the specific challenges, and the decoding

226 performance. Electrode discrimination ability (EDA) was assessed by calculating the percent

227 activation of each recording site of the electrode with respect to the different functional

228 challenges (see Methods for details and Supplementary Figures 3 and 4 for a graphical

229 example). In this way, the ensemble of channels activations forms a discrimination vector

230 for each functional challenge. Intuitively, the greater the difference between those

231 discrimination vectors representing different functional challenges, the more discriminative

232 is the electrode (Supplementary Fig.4b,c for distance matrices). We then calculated the

233 linear correlation coefficient between EDA and accuracy (Fig. 4b) and found a correlation

234 value, towards statistical significance, between electrode discrimination properties and

235 decoding performance (Fig. 4b Pearson correlation coefficients for accuracy vs. EDA $r =$

236 0.66 and $n = 4, p = 0.3$).

237

238 **A hybrid model framework to map the functional spatial organization of VN fascicles**

239 The site-related sensitivity to specific functional challenges indicated a possible functional

240 spatial organization of VN fascicles, which we explored by combining the information

241 obtained from histological analysis with simulations of electric potential field and

242 discrimination properties of the electrodes.

243 The spatial relationship between VN fascicles and electrode active sites was determined by

244 histological examination in one animal, p4 (see Methods for details). We reasonably assume

245 that the overall nerve morphology in terms of fascicular structure and organization is

246 constant along the implant site, so we morphologically modelled the SELINE active sites on

247 the same 2D transverse section representation of the VN (Fig. 5 panels a, b, left and middle

248 figures, for SELINEs s3 and s4 implanted in p4, respectively).

249 Based on the histological analysis, we constructed a hybrid modeling framework[38,39,41] to

250 understand the spatial distribution of electrical potential fields in the nerve sections of p4-s3

251 and p4-s4 (see Methods for details). In Supplementary Figures 5 and 6 (panel b),

252 isopotential electric field lines corresponding to each nerve section and 3 different recording

253 sites are shown (p4-s3 and p4-s4, respectively). Using the Helmholtz reciprocity theorem[41],

254 these potential values quantify the recording capability of a given active site favored by the

255 specific position of a fascicle located inside the nerve[42]. Since we were interested in the

256 global electrical activity of fascicles, we employed a mean field approach by averaging the

257 potential values within a given fascicle (Supplementary Figures 5 and 6 panel c, left) for

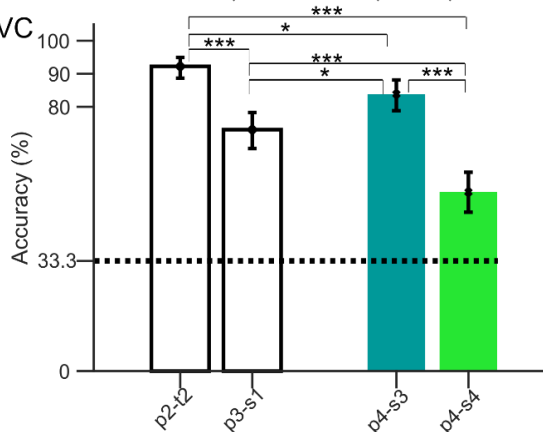258 nerve section p4-s3 and p4-s4, respectively.

Decoding Baseline vs. Two Challenges
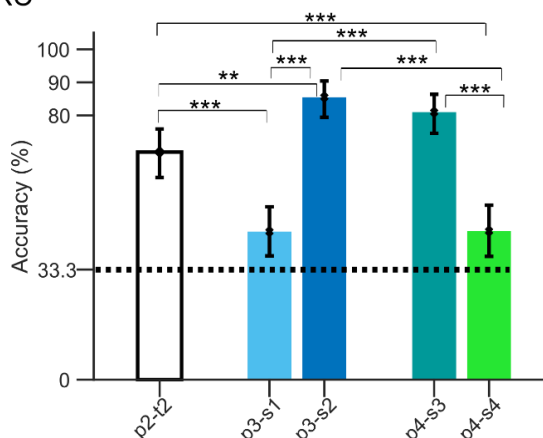
a Baseline vs. BPC vs. RRC

p2-t2=pig#2 implanted with TIME #2

p3-s1=pig#3 implanted with SELINE #1

p3-s2=pig#3 implanted with SELINE #2

p4-s3=pig#4 implanted with SELINE #3

p4-s4=pig#4 implanted with SELINE #4
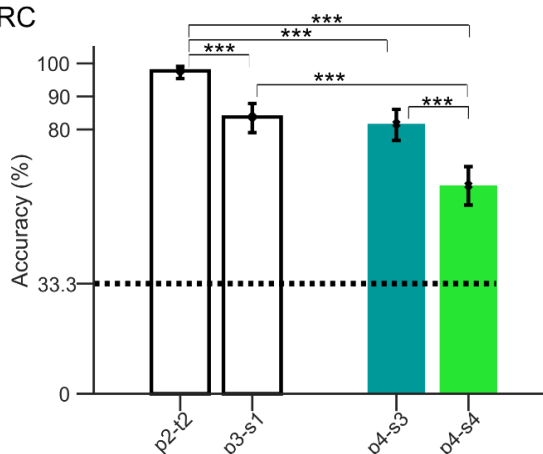
b Baseline vs. BPC vs. TVC

c Baseline vs. TVC vs. RRC

Fig. 3 Decoding accuracy for baseline condition vs. two functional challenges. Accuracy level together with confidence intervals (error bars, Clopper-Pearson method) for the comparison between baseline and BPC vs RRC (panel a), BPC vs TVC (panel b), RRC vs TVC (panel c). For all panels, colored bars indicate the same animal implanted with two different electrodes. Dashed lines represent chance level. Statistical comparisons between animals were assessed by using a Chi square test Bonferroni corrected for multiple comparisons (*p<0.05,**p<0.01,***p<0.001).

Decoding Baseline vs. Three Challenges
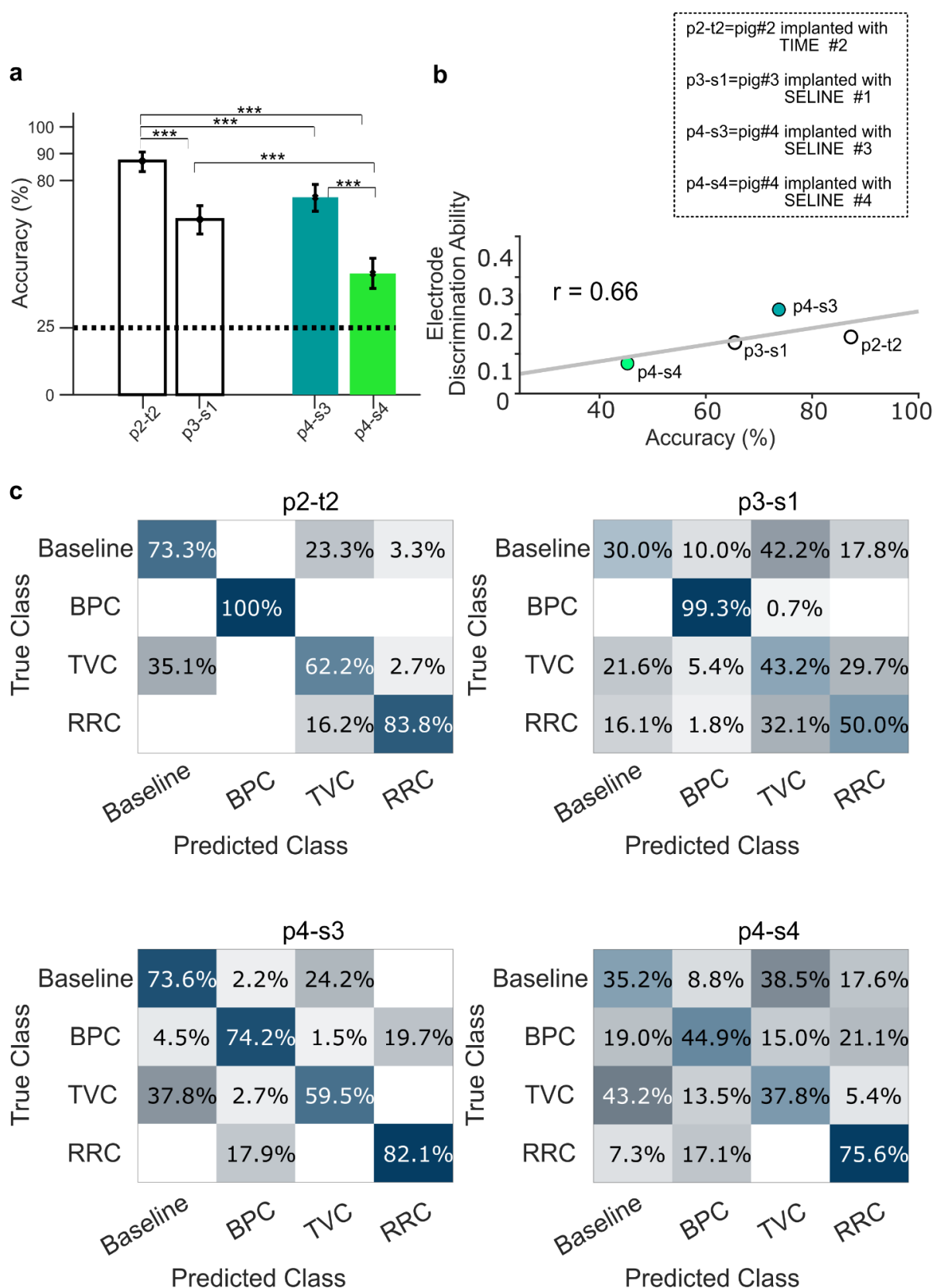
Fig. 4 Decoding accuracy for baseline condition vs. 3 functional challenges and relation between electrode discrimination ability and decoding performances. **a** Accuracy level together with confidence intervals (error bars, Clopper-Pearson method) for the comparison between baseline and BPC, TVC and RRC. Colored bars

270 indicate the same animal implanted with two different electrodes. Dashed lines represent chance levels.
271 Statistical comparisons between animals were assessed by using a Chi square test Bonferroni corrected for
272 multiple comparisons (*p<0.05, **p<0.01, ***p<0.001). **b** Linear relationship between electrode discrimination
273 ability and accuracy level, linear correlation coefficient is reported. **c** Confusion matrices for all the recordings.
274

275 To quantitatively characterize the association of a given fascicle with a specific functional

276 challenge, we weighted the discrimination index of each active site with the mean field

277 generated by that fascicle recorded from that active site. We then averaged data obtained

278 from all recording sites and normalized the average to the total mean field, thus obtaining

279 what we called Discriminative Field Potential (DFP, see Methods for details). In this way, we

280 developed for the first time a quantitative measure characterizing how a fascicle is related

281 to a given functional challenge. This measure could be considered the equivalent, for

282 recording, of the selectivity index[20,38] quantifying the stimulation ability on an electrode to

283 elicit the activation of targeted fibres.

284 DFP patterns related to baseline condition and functional challenges were obtained for each

285 nerve section p4-s3 and p4-s4, as shown in Figure 5 a,b, right panels, respectively, and

286 Supplementary Figures 5 and 6 panel c bottom, respectively. Interestingly, for both nerve

287 sections p4-s3 and p4-s4, the baseline condition exhibited a balanced DFP pattern where

288 each fascicle is activated in the same manner. On the contrary, DFP magnitude was higher

289 and differences between DFP patterns within each nerve were more pronounced in p4-s3

290 than in p4-s4 as shown in Figure 5 a,b, right panels, respectively, and Supplementary

291 Figures 5 and 6 panel c bottom, respectively. We quantified them by calculating the root

292 mean square level of the Euclidean distance among the DFP values of each fascicle for

293 each possible comparison between functional challenges (mean discriminative distance).

294 We found a statistically significant higher mean discriminative distance of the nerve in p4-

295 s3 with respect to p4-s4 (p=0.003 unpaired t-test, n=6 all possible functional challenges

296 combination). This was consistent with the higher effectiveness of decoding based on p4-

297 s3 recordings.
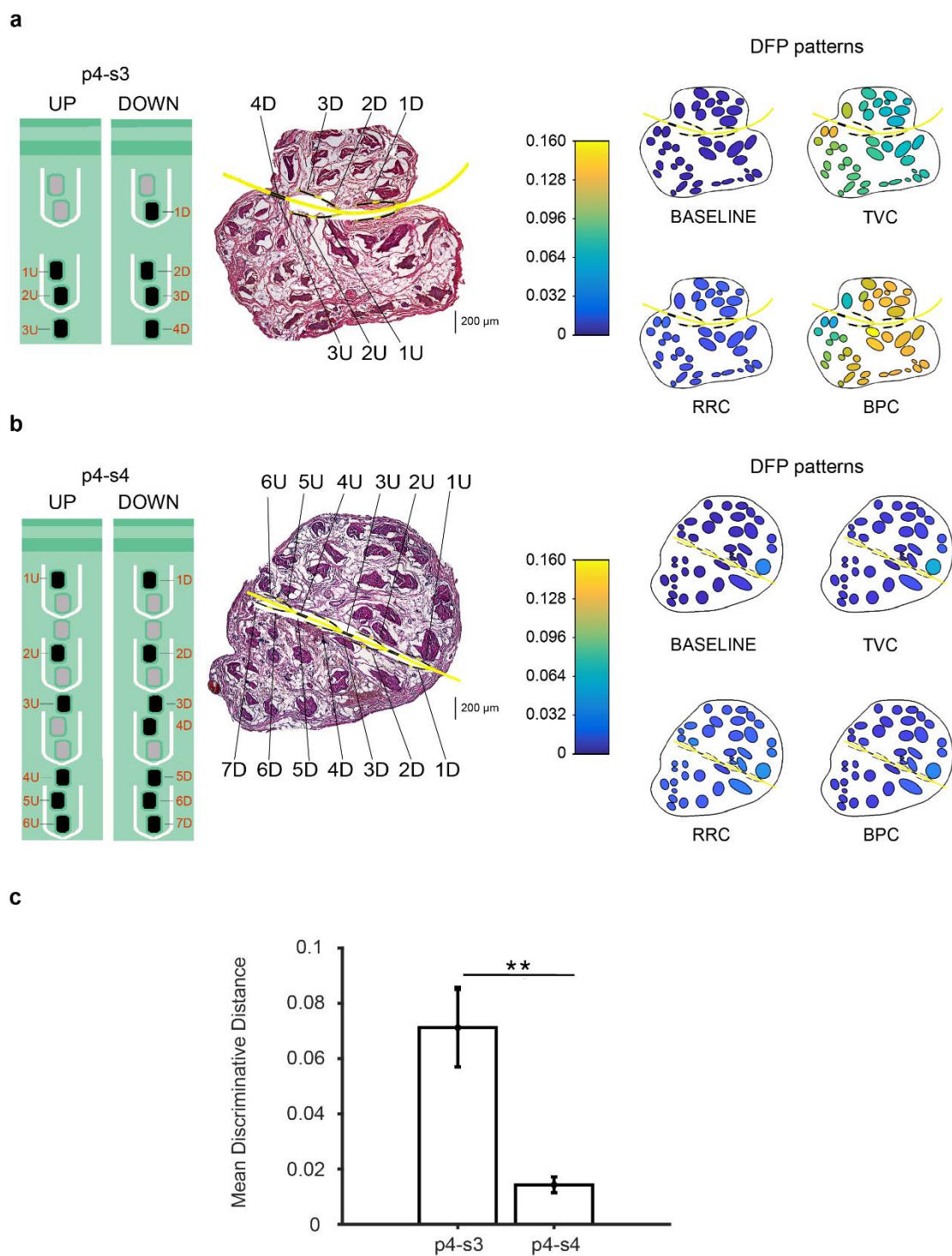
Fig. 5 Schematic description of the two SELINE (s3 and s4) implantation in the VN of p4 and hybrid model simulations of fascicles activation at baseline and in response to functional challenges. **a,b** SELINE s3 and s4 (left panels a,b, respectively) are represented on a VN histological section (central panels a,b respectively). DFP patterns of activity during baseline and each functional challenge (left panels). **c** Mean Discriminative Distance between DFP patterns (p=0.003 unpaired t-test n=6, p>0.05 Kolmogorov-Smirnov).

Discussion

Bioelectronic medicine may lead to revolutionary treatments for an ample variety of diseases. However, therapeutic neuromodulatory interventions must be very precise, both spatially, activating specific nerve fibres to avoid side effects, and temporally, i.e., operating in closed-loop to mimic the natural conditions. Therefore, it is necessary to utilize neural interfaces to selectively stimulate ANS nerves (spatial precision) and to decode signals triggered by specific functional changes, so that the stimulation is activated only when necessary (temporal precision) and subjected to a feedback control.

The present study provides the first evidence that signals recorded with intraneural electrodes in pig VN can be reliably used to detect functional changes in the cardiovascular and/or respiratory system.

We perturbed the homeostasis of one of both systems with functional challenges that were expected to enhance the activity of aortic baroreceptors and/or lung stretch receptors. Electrical signals departing from those receptors run along afferent fibres of the VN, carrying to the CNS information on blood pressure changes and lung inflation state[43]. Although induced with pharmacological and mechanical stimuli, these hemodynamic and respiratory alterations mimic very common pathophysiological conditions such as hypertension, tachypnea, and polypnea. Exploiting our previous experience with somatic nerves[31] and differently from previous studies[3,21,23,24,32] that employed spike sorting methods[23,24] or extracted neural profiles correlated with specific physiological variables[3,21,32], we considered the whole high frequency components of our signals processed with a novel advanced machine learning approach. This method proved successful in achieving high-level accuracy for the decoding of the functional challenges. In such regard, the pig VN is ideal for the development of clinically relevant technologies. The fascicular organization of pig VN is the closest to the complexity of human VN intraneural morphology compared to other species

332 commonly utilized in experimental research[44]. For instance, other studies have shown the

333 possibility to decode different functional challenges in the murine VN[23,24], which,

334 unfortunately, contains less fibres which are not subdivided in fascicles.

335 To the best of our knowledge, prior studies in pig VN[3,21,32] did not demonstrate the possibility

336 to decode multiple functional challenges. While cuff[3,21] and intraneural[32] electrodes in pigs

337 proved effective in extrapolating neural markers of blood pressure and respiratory activity,

338 no decoding analysis for the identification of mixed functional challenges was attempted.

339 Moreover, the recordings with cuff electrodes[3,21] were not obtained during the same

340 experimental session.

341 In this study we exploited intraneural (TIMEs and SELINEs) electrodes, which are conceived

342 to be transversally or obliquely inserted into the nerve, allowing spatially selective stimulation

343 and recording from different fascicles innervating distinct peripheral targets[45,46].Our results

344 show that the quality of decoding performances depends on the electrode position. This

345 could be due to the different functional role of fascicles adjacent to the recording sites and

346 prompts the hypothesis of a specific spatial segregation of vagal fibres traversed by specific

347 signals. Therefore, to map a possible spatial functional organization of VN fascicles, we

348 employed a hybrid modeling framework based on histological analysis combined with

349 electrodes discrimination ability properties. We assumed that the discrimination of a given

350 functional challenge in a specific recording site is higher when the local fibres are activated

351 by that specific stimulus and the local recording capability is high. Based on this assumption,

352 we developed a novel quantitative measure called Discriminative Field Potential (DFP),

353 obtaining distinct spatial configurations of discriminative patterns generated by fascicles

354 during the various functional challenges. It is important to note that the good reliability of

355 DFP patterns resulted from the use of intraneural electrodes, which potentially provide a

356 more accurate recording of the fascicles neural activity compared to epineural electrodes.

357   Moreover, placing a large number of active sites along the intraneural implant would

358   augment the interfaces with fascicles, thus reducing the number of implanted electrodes[29].

359   The present findings strongly suggest that multi-contact electrodes positioning is of crucial

360   importance for bioelectronic applications in a complex nerve such as the VN. In our opinion,

361   the development of an anatomical and electrophysiological in silico model of the VN would

362   be extremely useful to guide electrodes implantation and positioning and to overcome the

363   present limitations. In this regard, the pig VN represents an excellent model, given its

364   marked fasciculation, which likely reflects an equivalent high spatial segregation of fibres

365   innervating different peripheral sites.

366

367   **Limitations and future directions.** The present study was performed in an acute

368   experimental preparation and it is known that anesthesia exerts important effects on neural

369   activity and other physiological systems. For this reason, our next step will consist of

370   validating the implantation of intraneural electrodes for VN chronic recordings in non-

371   anesthetized animals. Moreover, our results seem to indicate that TIMEs could perform

372   better than SELINE, but more experiments are necessary to confirm these results. Finally,

373   another important step will be its implementation and validation of online signal analysis,

374   necessary for closed-loop VNS protocols.

375

376   **Conclusions.** The present results are an important step towards more precise

377   neuromodulation protocols based on the knowledge of specific patterns of neural activations

378   recordable in VN under physiological and pathological conditions. Advanced closed-loop

379   and spatially selective VNS could improve the treatment of pathological conditions by

380   selectively activating functionally specialized fibre fascicles, thus preventing the numerous

381   side-effects caused by the current technology.

382 The importance of understanding VN signals extends beyond VNS and closed-loop

383 applications. Being the biggest peripheral crossroad of signals between the CNS and

384 visceral organs, a sensitive and reliable technology for detection and decoding of VN activity

385 could serve for the diagnosis of pathophysiological conditions otherwise difficult to detect.

386 Deciphering the "vagal language" will also help clarifying the mechanisms by which VNS

387 exerts its curative effects and gaining deeper insights in the VN regulation of specific

388 physiological processes.

389

390

391

392

393

394

395

396

397

398

399

400

401

402

403

404

405

Materials and methods

Animals. This study was conducted in four castrated male farm pigs (*Sus Scrofa Domesticus*) 3-4-month old and weighing 28-30 kg. The animals were housed in the vivarium at room temperature (24°C) and fasted overnight before anesthesia with free access to water. All animal handling and experimental procedures were performed according to European Community guidelines (EC Council Directive 2010/63) and the Italian legislation on animal experimentation (Decreto Legislativo D.Lgs 26/2014).

Anesthesia and monitoring of physiological parameters. On the day of the experiment, pigs were anesthetized and prepared for surgery as previously described by us[47]. They were sedated with a cocktail of 4 mg/kg tiletamine hydrochloride and 4 mg/kg zolazepam hydrochloride injected intramuscularly, intubated and mechanically ventilated. The respiratory frequency was fixed to 10 respiratory cycles per minute and the tidal volume (TV) to 400 ml. The combination of these respiratory parameters resulted in $PaO_2 > 100$ mmHg, $PaCO_2 < 40$ mmHg and arterial blood pH in the range of 7.4-7.45. Arterial blood gases analysis was repeated at least every 30 min. A pulse oximeter was applied on the tongue to continuously monitor arterial oxygen saturation, which was stably above 96% for the duration of the experiment. Inhalatory anesthesia was maintained with a mixture of 1-1,5% isoflurane dissolved in 79% air and 21% oxygen. The respiratory pressure was recorded by connecting the airflow of the ventilator to a pressure transducer. Electrocardiogram (ECG), heart rate, and arterial blood pressure were constantly monitored. Aortic blood pressure was recorded using a solid-state pressure transducer catheter (Millar, SPR-100) inserted in the left femoral artery with the tip positioned in the abdominal aorta. This catheter was also used to withdraw arterial blood for blood gas analysis. Glycemia was checked every 30 min and

431   before each recording session to assess the stability of plasma glucose levels above 100

432   mg/100 ml. The main ear vein was cannulated for the intravenous administration of all the

433   drugs.

434

435   **Surgical preparation and electrode implantations.** The 4 pigs were named p1, p2, p3

436   and p4. To isolate the cervical VN, a midline cervical incision was made from the level of the

437   larynx to the sternum, as previously described by us[48]. After identifying the neurovascular

438   bundle of the neck (common carotid artery, internal jugular vein and VN), the left (n = 3) and

439   right (n = 1) cervical VNs were delicately separated from the common carotid artery by blunt

440   dissection, 3-4 cm above and below the cricoid cartilage. The sympathetic trunk, attached

441   dorsally to the VN, was gently detached and pulled apart. In animals p1 and p2, the left VN

442   was implanted in correspondence of the cricoid cartilage with a transverse intrafascicular

443   multichannel electrode (TIME) endowed with 10 active sites, following the same procedures

444   described by Badia et al[49]. In p3 and p4, the left and right VNs, respectively, were implanted

445   with 2 self-opening intraneural peripheral interfaces (SELINEs) endowed with 7-16 active

446   sites. SELINEs implantation followed the same procedures described by Cutrone et al[46]. All

447   the intraneural electrodes were inserted obliquely, forming a 45° angle with the longitudinal

448   axis of the nerve, except for 2 SELINEs, one in p3 and one in p4, that were inserted along

449   the transverse axis. In all the experiments, the ground electrode was inserted under the skin

450   of the left elbow of the animal.

451

452   **Tissue isolation and histology.** At the end of the experiment, the anesthetized pigs were

453   euthanized by an intravenous injection of saturated KCl solution. Intraneural electrodes were

454   left in place and the VN was cut 3 cm above and below the insertion site and gently placed

455   on a dedicated support to avoid twisting. The VN samples were then fixed in 4%

456 paraformaldehyde for 18-20 hours, rinsed in PBS, dehydrated in a series of progressively

457 more concentrated solutions of ethanol/xylol and finally embedded in paraffin wax.

458 Transverse sections (10 µm thick) were cut, deparaffinized, rehydrated, processed for

459 routine hematoxylin and eosin and mounted in silane-coated slides. Images were captured

460 with 5x magnification by a Leica DMRB microscope equipped with the DFC480 digital

461 camera (Leica Microsystems, Cambridge, UK). Sections at the level of the implanted

462 electrodes were aligned and manually segmented to study the electrode–nerve interaction.

463 The nerve was cross-sectioned for the entire length of the implants, with the two SELINEs

464 fixed in site, and stained with hematoxylin and eosin. Light microscopy observations of VN

465 sections showed the fascicular structure of the nerve and holes caused by the electrode

466 insertion, with SELINE polyimide strips preserved in a few slices. No macroscopic and

467 microscopic signs of hemorrhages were found.

468

469 **In vivo recording of VN activity.** Neural recordings started at least 30 min after electrode

470 implantation to allow for stabilization of the nerve and of physiological parameters. The

471 neural signals were first acquired over 5 minutes at baseline, followed by recording sessions

472 in which physiological parameters were altered (functional challenges). The baseline

473 condition was defined as the time BP and heart rate were found stable for at least 30 min

474 after completion of electrodes implantation. At baseline, RR and TV were fixed at 10

475 respiratory cycles per minute and 400 ml, respectively. The functional challenges consisted

476 of 1) increase in mean arterial BP up to 150% of the baseline value obtained with an

477 intravenous infusion of Ang II (Sigma Aldrich), a vasopressor with rapidly reversible

478 effects[50], at 80 ng/kg/min 2) increase in TV from 400 to 500 in p2 and 800 ml in p3 and p4

479 for 2 minutes and 3) increase in RR from 10 to 15 in p2 and 20 in p3 and p4 respiratory

480 cycles/min. These challenges were produced in random order and each one was followed

481   by a recovery period of at least five minutes to let the physiological parameters return to

482   baseline values. These functional challenges and the related physiological parameters

483   affected were in the same range of the ones used by Sevcencu et al.[21] and proved suitable

484   for neural VN recordings in anesthetized pigs. In addition, they did not interfere significantly

485   with the stability of other variables like BP, heart rate or blood gases partial pressures.

486   Glycemia and blood gases were checked before and after the completion of each functional

487   challenge.

488

489   **Data acquisition and decoding algorithm.** VN raw multichannel signals were acquired at

490   a frequency sampling of 24.4 kHz, high pass filtered at 5 Hz and digitally amplified (RZ5D

491   BioAmp Processor, Pz5, Tucker-Davis Technologies Inc., TDT, USA). Each channel of the

492   raw recordings was segmented by using a 1 sec-temporal window and rescaled to zero

493   mean and unitary standard deviation. Discrete wavelet transform[33,34], at a maximum level

494   equal to 4, was applied on the segmented portions of each channel by using a symlet 7

495   wavelet function[13,33,34]. Approximation coefficients relative to frequencies $\lessgtr$ 1500 Hz were

496   discarded in the subsequent analysis. Principal component analysis on the multivariate

497   wavelet details was applied independently on two different scales[35] relative to frequency

498   ranges of $\cong$1500-3000 Hz and 3000-6000 Hz, respectively. The first three principal

499   components were retained to build a feature vector for the classification algorithm. The

500   entire dataset was randomly split in 70 % for the train set and the remaining 30% was used

501   as test set. Ensemble of classifiers were built using a classification tree[36,37]. To deal with

502   class imbalance problems, random undersampling techniques combined with boosting

503   algorithms were adopted (RUSBoost)[37,51]. To achieve higher ensemble accuracy, we set

504   the maximal depth of the decision tree equal to the number of the element in the train set.

505 We set the learning rate and the number of cycles to 0.1 and 1000, respectively, in order to

506 achieve higher accuracy as well.

507 Classification performance was assessed on the test set by calculating accuracy of the

508 corresponding confusion matrices. The accuracy level was calculated by considering the

509 number of correct predictions divided by the total number of elements in the test set.

510 Confidence intervals for accuracy values were computed by using Clopper-Pearson method.

511 Chance level was estimated as the proportion of the class with the majority of elements with

512 respect to the total number of elements.

513 Data were analyzed off-line in MATLAB (The MathWorks, Inc.).

514

515 **Discrimination analysis and decoding-discrimination relationship.** Similarly to previous

516 studies[20], we built a discrimination channel index to understand the discrimination ability of

517 the electrodes and consequentially a possible relation with decoding performances. To this

518 aim, we calculated the percentage of activation for each channel relative to the different

519 functional challenges as described below.

520 For each challenge, each signal was reconstructed using the wavelet details at the same

521 scale previously used for the decoding algorithm:

$$x_s(t) \approx \sum_{j=1}^{2} \sum_{k} d_{s,j}[k] * \psi_{jk}(t)$$

523 where $d_{s,j}[k]$ are the wavelet details at scale j of the recording site s, and $\psi_{jk}(t)$ is the

524 wavelet function (see Supplementary Figure 3a,b for a graphical example). The

525 reconstructed signals from each recording sites $(X = \{x_s\},\ i = 1,\dots,S)$ were segmented

526 using a temporal window of T=1 sec and rescaled to zero mean and unitary standard

527 deviation obtaining a number of signal's blocks N_{block}, i.e. $X = (X(1),\dots,X(N_{block}))$. For

528 each block of the signals, we calculated the first three principal component coefficients

529 (loadings), i.e. $P^{i_{pca}}(i_{block})$ with $i_{pca} = 1,2,3$ and $i_{block} = 1, \dots , N_{block}$. We thus identified for

530 each principal component the higher outliers relative to loadings' absolute values. Outliers

531 were identified using a threshold of three scaled mean absolute deviation from the median

532 (see Supplementary Figure 3c, right panel for a graphical example). When an outlier was

533 identified in a portion of the signal, a value equal to unity was assigned to the corresponding

534 channel ('channel activated') and zero otherwise, i.e. we defined an indicator for each

535 channel s and block i_{block}:

536

$$I_s^{i_{pca}}(i_{block}) = \begin{cases} 1 & if\ loading\ of\ i_{pca}\ w.r.t.\ channel\ s\ is\ outlier \\ 0 & otherwise \end{cases}$$

537

538

539 For each channel, the resulting percentage of activation relative to a principal component

540 $\mu_s^{i_{pca}}$, is equal to the number of times in which the channel was activated divided by the total

541 number of portions of the signal, i.e.

$$\mu_s^{i_{pca}} = \frac{\sum_{i_{block}=1}^{N_{block}} I_s^{i_{pca}}(i_{block})}{N_{block}}$$

542

543 The percentage of activation of each channel was quantified as the mean over the

544 percentage of activation of the channel in each principal component (see Supplementary

545 Figure 3c left panel) $\mu_s = \frac{\sum_{i_{pca}=1}^{3} \mu_s^{i_{pca}}}{3}$.

546 Similarly to Raspopovic et. al[20], given the percentage of activation for each channel, we

547 defined a discrimination index for each channel as the difference between the percentage

548 of activation of the considered channel and the mean percentage of activation over the

549 remaining channels, i.e.

550
$$D_s = \mu_s - \frac{1}{N_s - 1} \sum_{s=1, i \neq l}^{N_s} \mu_l.$$

551 Thus, discrimination vectors with entries made of channels' discrimination indices were

552 obtained among the different functional challenges, i.e. $D_c = \{D_{c,s}\}$ with $c =$

553 $\{Baseline, BPC, TVC, RRC\}$ and $s = 1, \dots, S$. The difference between two generic

554 discrimination vectors was obtained by considering the root mean square level of the

555 Euclidean distance (see Supplementary Figure 4a).

556 Electrode discrimination ability was computed by considering the mean over all the six

557 possible combination distances between the distinct discrimination vectors (see

558 Supplementary Figure 4a). Finally, a linear correlation coefficient was calculated between

559 the electrode discrimination ability and the decoding performance (accuracy) and the least-

560 squares line was plotted.

561

562 **Hybrid modelling of the recording process and Discriminative Field Potentials.** To

563 understand the distribution of the electrical field potential within a nerve, we employed the

564 hybrid modeling framework as described in [38,39,41]. Histological sections were manually

565 segmented by defining the contours of the epineural compartment (the whole nerve section

566 contour) and of the fascicles. Such contours were imported in MATLAB as closed polylines.

567 Fascicle polylines were substituted with ellipses having the same surface area as the

568 fascicles, center of the fascicle centroid, axis length ratio and orientation were deduced from

569 the minimum (area) bounding rectangle of each fascicle. The perineurial sheath for each

570 fascicle was defined as a layer with width equal to 0.03 times the effective diameter

571 (diameter of the equivalent circle) of the fascicle[52]. A 3D extrusion of the given nerve section

572 was defined in COMSOL (through MATLAB LiveLink for COMSOL) and it was included in a

573 saline bath whose external surface was grounded (simulation of zero potential at infinity [39]).

574   A point current source was defined corresponding to each electrode active site center. To

575   obtain the potential field on the nerve section (up to a multiplicative scaling factor, i.e.

576   linearity assumption), we simulated the stimulation from all given sites with an adimensional

577   current (one at the time and unitary). Indeed, thanks to the Helmholtz reciprocity theorem,

578   the value of the potential field due to a unitary current injected by an active site corresponds

579   to the impedance that relates the intensity of a current source with the resulting potential

580   field recorded at the site surface. This means that a higher electrical field in a point in space

581   P leads to a higher amplitude of the recorded electrical activity of a fibre located in P [42].

582   Given the knowledge of the electric field potential generated from a fascicle and the

583   corresponding recording capability of a given recording site, we wanted to link this

584   information to the discrimination properties of the recording site. To this aim, we defined a

585   measure, that we called Discriminative Field Potential (DFP), by weighting the recording

586   capabilities of a recording site *s* from a given fascicles *F* together with the discrimination

587   properties of the recording site *s* related to a functional challenge *c*, i.e.

588
$$DFP_{c,F} = \frac{\sum_{s=1}^{S} D_{c,s} \, \varphi_{s,F}}{\sum_{s=1}^{S} \varphi_{s,F}}$$

589   where $D_{c,s}$ is the discrimination ability to a functional challenge *c* and recording site s, and

590     $\varphi_{s,F}$ is the mean field inside a fascicle *F* recorded from a site *s* (calculated by averaging

591   isopotential values of the potential field inside the fascicle) . Since the $\varphi_{s,F}$ measures how

592   a site *s* is capable of recording from a given fascicle, and $D_{c,s}$ measures how site *s* records

593   better the activity related to a functional challenge *c* with respect to the other sites, then the

594     $DFP_{c,F}$ is a quantity measuring how a fascicle is related to a given functional challenge.

595   Similarly to the calculation of electrode discrimination ability, to quantify the discrimination

596   ability of the whole nerve section, we computed the root mean square level of the Euclidean

597   distance of the DFP values in the fascicle space. We thus calculated the mean

598   discrimination distance by considering the mean over all the six possible combinations of

599   functional challenges.

600   **Statistical analysis.**   Unless otherwise stated, data are expressed as mean ± s.e.m.

601   Statistical significance between accuracies were assessed by means of Chi square test

602   Bonferroni corrected for multiple comparisons. Confidence intervals for the accuracy values

603   were calculated using the Clopper-Pearson method. Statistical significance of accuracy

604   values with respect to chance level was assessed by using the binomial test. Statistical

605   significance between the discrimination ability of nerve sections was assessed by using two-

606   tailed unpaired t-test at a significance threshold equal to 0.05. To test for normality of data

607   distribution a Kolmogorov-Smirnov test was used on each population of data. Statistical

608   analysis was performed with MATLAB (The MathWorks, Inc.).

609

610

611

612

613

614

615

616

617

618

References

1. Birmingham, K. *et al.* Bioelectronic medicines: A research roadmap. *Nat. Rev. Drug Discov.* **13**, 399–400 (2014).

2. Famm, K., Litt, B., Tracey, K. J., Boyden, E. S. & Slaoui, M. A jump-start for electroceuticals. *Nature* **496**, 159–161 (2013).

3. Sevcencu, C., Nielsen, T. N. & Struijk, J. J. A neural blood pressure marker for bioelectronic medicines for treatment of hypertension. *Biosens. Bioelectron.* **98**, 1–6 (2017).

4. Johnson, R. L. & Wilson, C. G. A review of vagus nerve stimulation as a therapeutic intervention. *J. Inflamm. Res.* **11**, 203–213 (2018).

5. George, R. *et al.* A randomized controlled trial of chronic vagus nerve stimulation for treatment of medically intractable seizures. *Neurology* **45**, 224–230 (1995).

6. Klein, H. U. & De Ferrari, G. M. Vagus nerve stimulation: A new approach to reduce heart failure. *Cardiol. J.* **17**, 638–643 (2010).

7. Koopman, F. A. *et al.* Vagus nerve stimulation inhibits cytokine production and attenuates disease severity in rheumatoid arthritis. *Proc. Natl. Acad. Sci.* **113**, 8284–8289 (2016).

8. Bonaz, B. *et al.* Chronic vagus nerve stimulation in Crohn's disease: A 6-month follow-up pilot study. *Neurogastroenterol. Motil.* **28**, 948–953 (2016).

9. Yuan, H. & Silberstein, S. D. Vagus Nerve and Vagus Nerve Stimulation, a Comprehensive Review: Part II. *Headache* **56**, 259–266 (2016).

10. Tracey Kevin J. The inflammatory reflex. *Nature* **257**, 122–125 (2005).

11. Meyers, E. C. *et al.* Vagus nerve stimulation enhances stable plasticity and generalization of stroke recovery. *Stroke* **49**, 710–717 (2018).

643   12.   J.P., B., T., B., Beekwilder, J. P. & Beems, T. Overview of the clinical applications of

644   vagus nerve stimulation. *J. Clin. Neurophysiol.* **27**, 130–138 (2010).

645   13.   Citi, L. *et al.* On the use of wavelet denoising and spike sorting techniques to

646   process electroneurographic signals recorded using intraneural electrodes. *J.*

647   *Neurosci. Methods* **172**, 294–302 (2008).

648   14.   Ganzer, P. D. & Sharma, G. Opportunities and challenges for developing closed-

649   loop bioelectronic medicines. *Neural Regen. Res.* **14**, 46–50 (2019).

650   15.   Zanos, S. Closed-Loop Neuromodulation in Physiological and Translational

651   Research. *Cold Spring Harb. Perspect. Med.* a034314 (2018)

652   doi:10.1101/cshperspect.a034314.

653   16.   Micera, S., Carpaneto, J. & Raspopovic, S. Control of hand prostheses using

654   peripheral information. **3**, 48–68 (2010).

655   17.   Sun, F. T. & Morrell, M. J. Closed-loop Neurostimulation: The Clinical Experience.

656   *Neurotherapeutics* **11**, 553–563 (2014).

657   18.   Bouton, C. Neural decoding and applications in bioelectronics medicine. *Bioelectron.*

658   *Med.* **2**, 20–24 (2015).

659   19.   Xue, N., Martinez, I. D., Sun, J., Cheng, Y. & Liu, C. Flexible multichannel vagus

660   nerve electrode for stimulation and recording for heart failure treatment. *Biosens.*

661   *Bioelectron.* **112**, 114–119 (2018).

662   20.   Raspopovic, S., Capogrosso, M., Badia, J., Navarro, X. & Micera, S. Experimental

663   validation of a hybrid computational model for selective stimulation using transverse

664   intrafascicular multichannel electrodes. *IEEE Trans. Neural Syst. Rehabil. Eng.* **20**,

665   395–404 (2012).

666   21.   Sevcencu, C., Nielsen, T. N., Kjærgaard, B. & Struijk, J. J. A Respiratory Marker

667   Derived From Left Vagus Nerve Signals Recorded With Implantable Cuff Electrodes.

Neuromodulation **21**, 269–275 (2017).

22. Metcalfe, B. W., Nielsen, T. N., Donaldson, N. de N., Hunter, A. J. & Taylor, J. T. First demonstration of velocity selective recording from the pig vagus using a nerve cuff shows respiration afferents. *Biomed. Eng. Lett.* **8**, 127–136 (2018).

23. Zanos, T. P. *et al.* Identification of cytokine-specific sensory neural signals by decoding murine vagus nerve activity. *Proc. Natl. Acad. Sci. U. S. A.* **115**, E4843--E4852 (2018).

24. Battinelli, E. *et al.* Identification of hypoglycemia-specific neural signals by decoding murine vagus nerve. *Bioelectron. Med.* **115**, E4843–E4852 (2018).

25. Cracchiolo, M. *et al.* Decoding Neural Metabolic Markers From the Carotid Sinus Nerve in a Type 2 Diabetes Model. **27**, 2034–2043 (2019).

26. Navarro, X. *et al.* A Critical Review of Interfaces with the Peripheral Nervous System for the Control of Neuroprotheses and Hybrid Bionic Systems. *J Peripher Nerv Syst* **10**, 229–258 (2005).

27. Raspopovic, S., Carpaneto, J., Udina, E., Navarro, X. & Micera, S. On the identification of sensory information from mixed nerves by using single-channel cuff electrodes. *J. Neuroeng. Rehabil.* **7**, 1–15 (2010).

28. Rozman, J. & Ribarič, S. Selective recording of electroneurograms from the left vagus nerve of a dog during stimulation of cardiovascular or respiratory systems. *Chin. J. Physiol.* **50**, 240–250 (2007).

29. Micera, S. *et al.* Decoding of grasping information from neural signals recorded using peripheral intrafascicular interfaces. *J. Neuroeng. Rehabil.* **8**, 53 (2011).

30. Rossini, P. M. *et al.* Double nerve intraneural interface implant on a human amputee for robotic hand control. *Clin. Neurophysiol.* **121**, 777–783 (2010).

31. Cracchiolo, M. *et al.* Decoding of grasping tasks from intraneural recordings in trans-

693   radial amputee. *J. Neural Eng.* 0–35 (2020) doi:10.1088/1741-2552/ab8277.

694   32.   Sevcencu, C., Nielsen, T. N. & Struijk, J. J. An Intraneural Electrode for Bioelectronic

695   Medicines for Treatment of Hypertension. *Neuromodulation* **21**, 777–786 (2018).

696   33.   Mallat, S. *A Wavelet Tour of Signal Processing. A Wavelet Tour of Signal*

697   *Processing* (Elsevier Inc., 2009). doi:10.1016/B978-0-12-374370-1.X0001-8.

698   34.   Mallat, S. G. A Theory for Multiresolution Signal Decomposition: The Wavelet

699   Representation. *IEEE Trans. Pattern Anal. Mach. Intell.* **11**, 674–693 (1989).

700   35.   Bakshi, B. R. Multiscale PCA with application to multivariate statistical process

701   monitoring. *AIChE J.* **44**, 1596–1610 (1998).

702   36.   Breiman, L., Friedman, J. H. (Jerome H. ., Olshen, R. A. & Stone, C. J. *Classification*

703   *and regression trees.*

704   37.   Hastie, Trevor, Tibshirani, Robert, Friedman, J. *The Elements of Statistical Learning*

705   *The Elements of Statistical LearningData Mining, Inference, and Prediction, Second*

706   *Edition. Springer series in statistics* (2009). doi:10.1007/978-0-387-84858-7.

707   38.   Raspopovic, S., Capogrosso, M. & Micera, S. A computational model for the

708   stimulation of rat sciatic nerve using a transverse intrafascicular multichannel

709   electrode. *IEEE Trans. Neural Syst. Rehabil. Eng.* **19**, 333–344 (2011).

710   39.   Raspopovic, S., Petrini, F. M., Zelechowski, M. & Valle, G. Framework for the

711   Development of Neuroprostheses: From Basic Understanding by Sciatic and Median

712   Nerves Models to Bionic Legs and Hands. *Proc. IEEE* **105**, 34–49 (2017).

713   40.   Boretius, T. *et al.* A transverse intrafascicular multichannel electrode (TIME) to

714   interface with the peripheral nerve. *Biosens. Bioelectron.* **26**, 62–69 (2010).

715   41.   Simone Romeni, Giacomo Valle, Alberto Mazzoni, S. M. Tutorial: A computational

716   framework for the design and optimization of peripheral neural interfaces. *Nat.*

717   *Protoc.* **in press**, (2020).

718   42.   Jehenne, B., Raspopovic, S., Capogrosso, M., Arleo, A. & Micera, S. Recording

719   properties of an electrode implanted in the peripheral nervous system: A human

720   computational model. *Int. IEEE/EMBS Conf. Neural Eng. NER* **2015**-**July**, 482–485

721   (2015).

722   43.   Paintal, A. S. Vagal sensory receptors and their reflex effects. *Physiol. Rev.* **53**,

723   159–227 (1973).

724   44.   Settell, M. L. *et al.* Functional Vagotopy in the Cervical Vagus Nerve of the Domestic

725   Pig : Implications for Vagus Nerve Stimulation. 1–28 (2019).

726   45.   Gaillet, V. *et al.* Spatially selective activation of the visual cortex via intraneural

727   stimulation of the optic nerve. *Nat. Biomed. Eng.* (2019) doi:10.1038/s41551-019-

728   0446-8.

729   46.   Cutrone, A. *et al.* A three-dimensional self-opening intraneural peripheral interface

730   ({SELINE}). *J. Neural Eng.* **12**, 16016 (2015).

731   47.   Gabisonia, K. *et al.* MicroRNA therapy stimulates uncontrolled cardiac repair after

732   myocardial infarction in pigs. *Nature* **569**, 418–422 (2019).

733   48.   Labinskyy, V. *et al.* Chronic activation of peroxisome proliferator-activated receptor-α

734   with fenofibrate prevents alterations in cardiac metabolic phenotype without

735   changing the onset of decompensation in pacing-induced heart failure. *J.*

736   *Pharmacol. Exp. Ther.* **321**, 165–171 (2007).

737   49.   Badia, J., Raspopovic, S., Carpaneto, J., Micera, S. & Navarro, X. Spatial and

738   functional selectivity of peripheral nerve signal recording with the transversal

739   intrafascicular multichannel electrode (TIME). *IEEE Trans. Neural Syst. Rehabil.*

740   *Eng.* **24**, 20–27 (2016).

741   50.   Recchia, F. A. *et al.* Reduced synthesis of NO causes marked alterations in

742   myocardial substrate metabolism in conscious dogs. *Am. J. Physiol. - Endocrinol.*

743   *Metab.* **282**, 197–206 (2002).

744 51. Galar, M., Fernandez, A., Barrenechea, E., Bustince, H. & Herrera, F. A review on

745   ensembles for the class imbalance problem: Bagging-, boosting-, and hybrid-based

746   approaches. *IEEE Trans. Syst. Man Cybern. Part C Appl. Rev.* **42**, 463–484 (2012).

747 52. Grinberg, Y., Schiefer, M. A., Tyler, D. J. & Gustafson, K. J. Fascicular perineurium

748   thickness, size, and position affect model predictions of neural excitation. *IEEE*

749   *Trans. Neural Syst. Rehabil. Eng.* **16**, 572–581 (2008).

750

751

752

753

754

755

756

757

758

759

760

761

762

763

764

765

766

767

768

769

770

771

Supplementary Information:

Simultaneous decoding of cardiovascular and respiratory functional changes from pig intraneural vagus nerve signals

Supplementary Figure 1. Confusion matrices between baseline condition against one functional challenge a,b,c. Comparison between baseline and BPC (panel a), RRC (panel b), TVC (panel c).

Supplementary Figure 2. Confusion matrices between baseline condition against two functional challenges a,b,c Comparison between baseline and BPC-RRC (panel a), BPC-TVC (panel b), RRC-TVC (panel c).

Supplementary Figure 3. Discrimination analysis method. a Raw recording. **b** Signal in the frequency band 1500-6000 Hz reconstructed throughout wavelet details used in the decoding algorithm (segmented in a temporal window of 1 sec). **c** Estimation of channels discrimination index. Right panel, outlier detection on PCA loadings for the different functional challenges. Left panel, schematic representation of the active sites in the electrode p4-s3 and percentage of activation level estimation in single channels.

Supplementary Figure 4. Estimation of electrode discrimination ability and RMS level distance matrices examples. a Estimation of electrode discrimination ability. Left panel, 3D graphical visualization example of discrimination index channel vectors for TVC and BPC challenges (green and yellow vectors, respectively). Middle panel, root mean square level distance matrix. Right panel, estimation of electrode discrimination ability by averaging over all possible (n=6) combination comparison of functional challenge.

b,c RMS level distance matrices in the electrode discrimination space for the comparison among baseline condition and the functional challenges (TVC, RRC, BPC) in two electrodes placed in different animals (p2-t2 and p3-s1) and two electrodes in the same animal (p4-s3 and p4-s4), respectively.

Supplementary Figure 5 and 6. Discriminative Field Potential (DFP) estimation in pig p4e1 and p4e2, respectively. a Nerve cross-section and implanted electrode. The intraneural fascicles numerical are labeled with numbers i=1,…,$N_{fascicles}$. **b** Isopotential Electric field lines for three different recording sites. **c** DFP estimation procedure. Left panel, fascicle mean field for each site. Right panel, selectivity index for each site across the different functional challenges. Bottom panel, DFP values in each fascicle across the different functional challenges.

820 **Supplementary Figure 1**
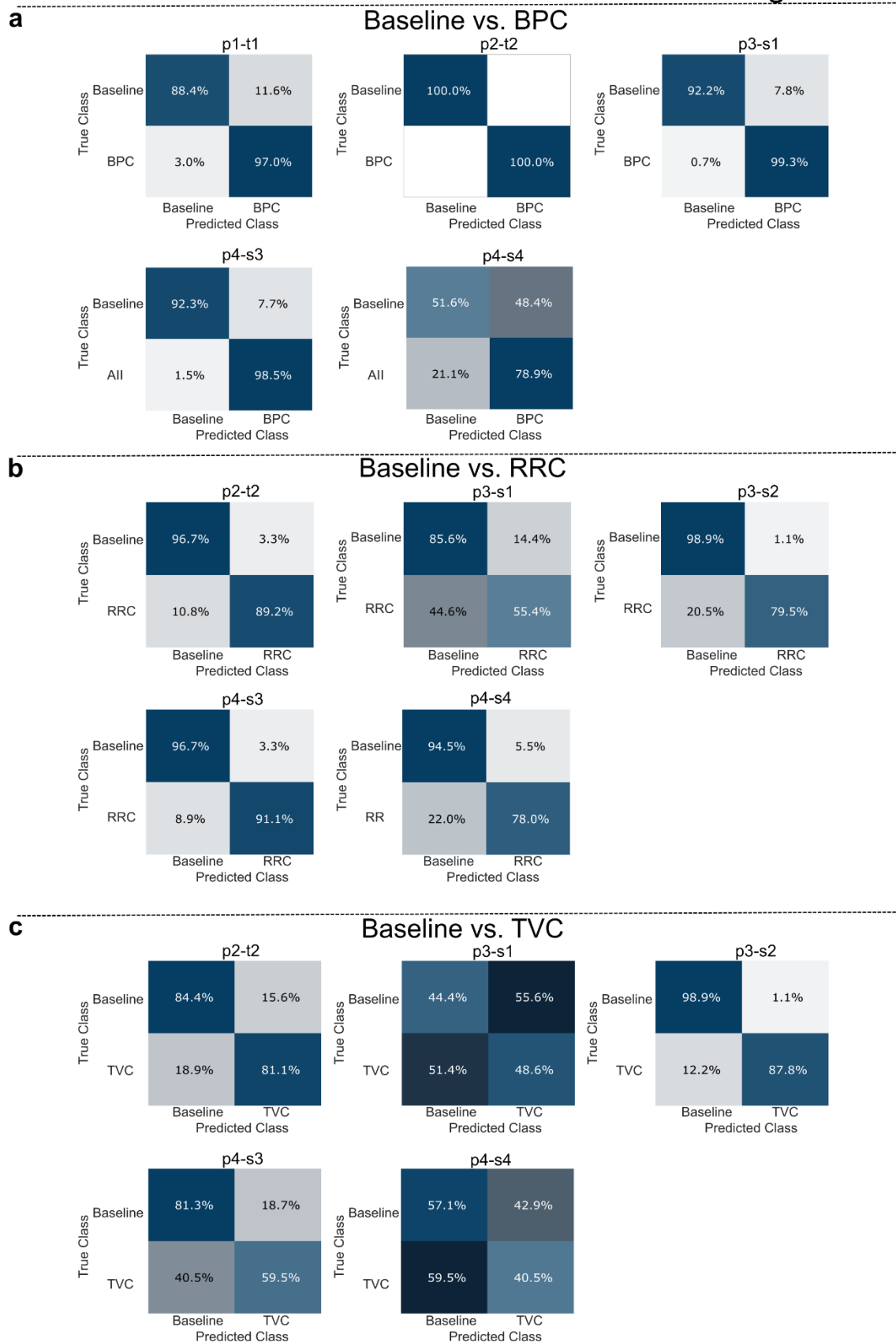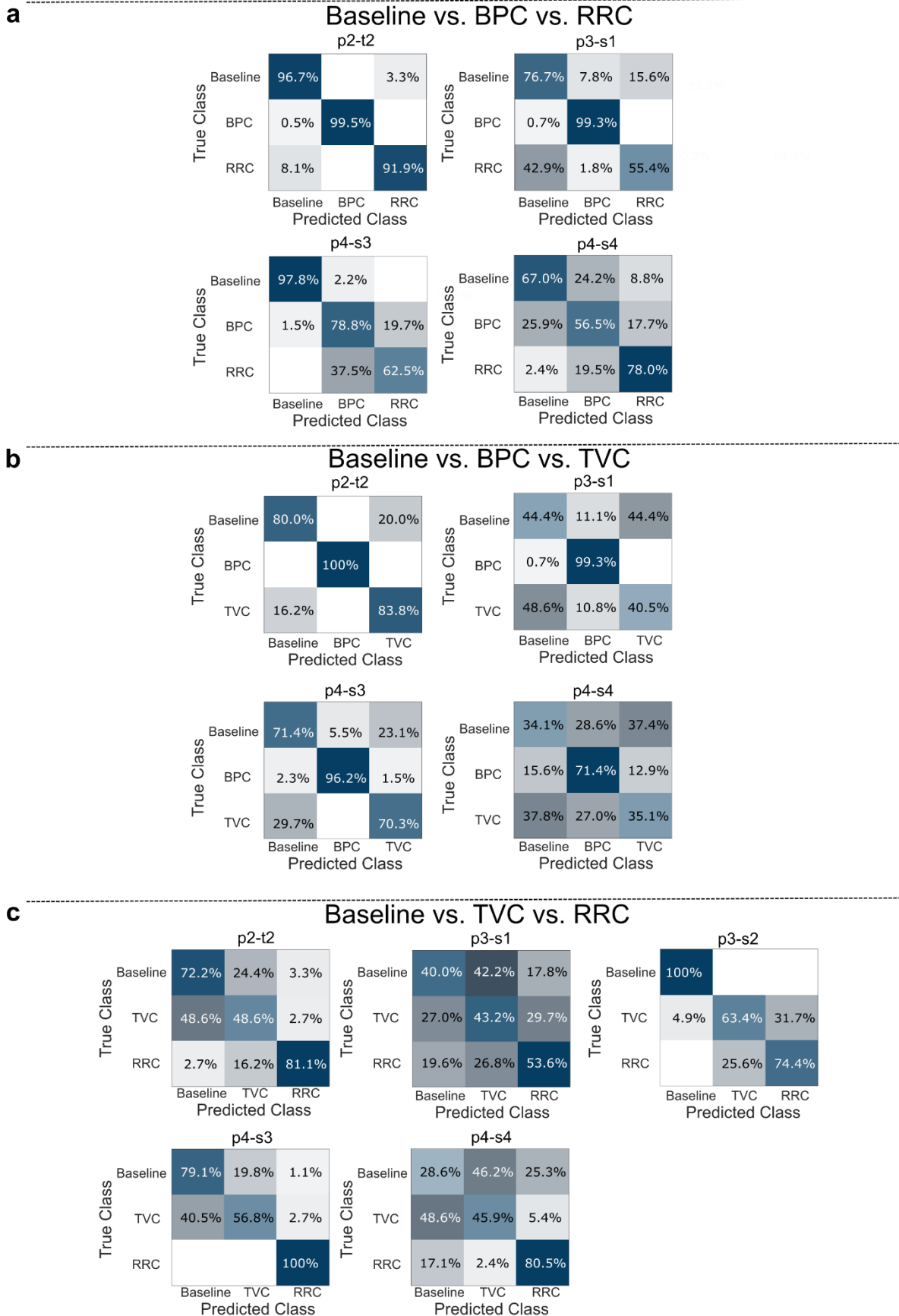

Confusion Matrices Baseline vs. One Challenge
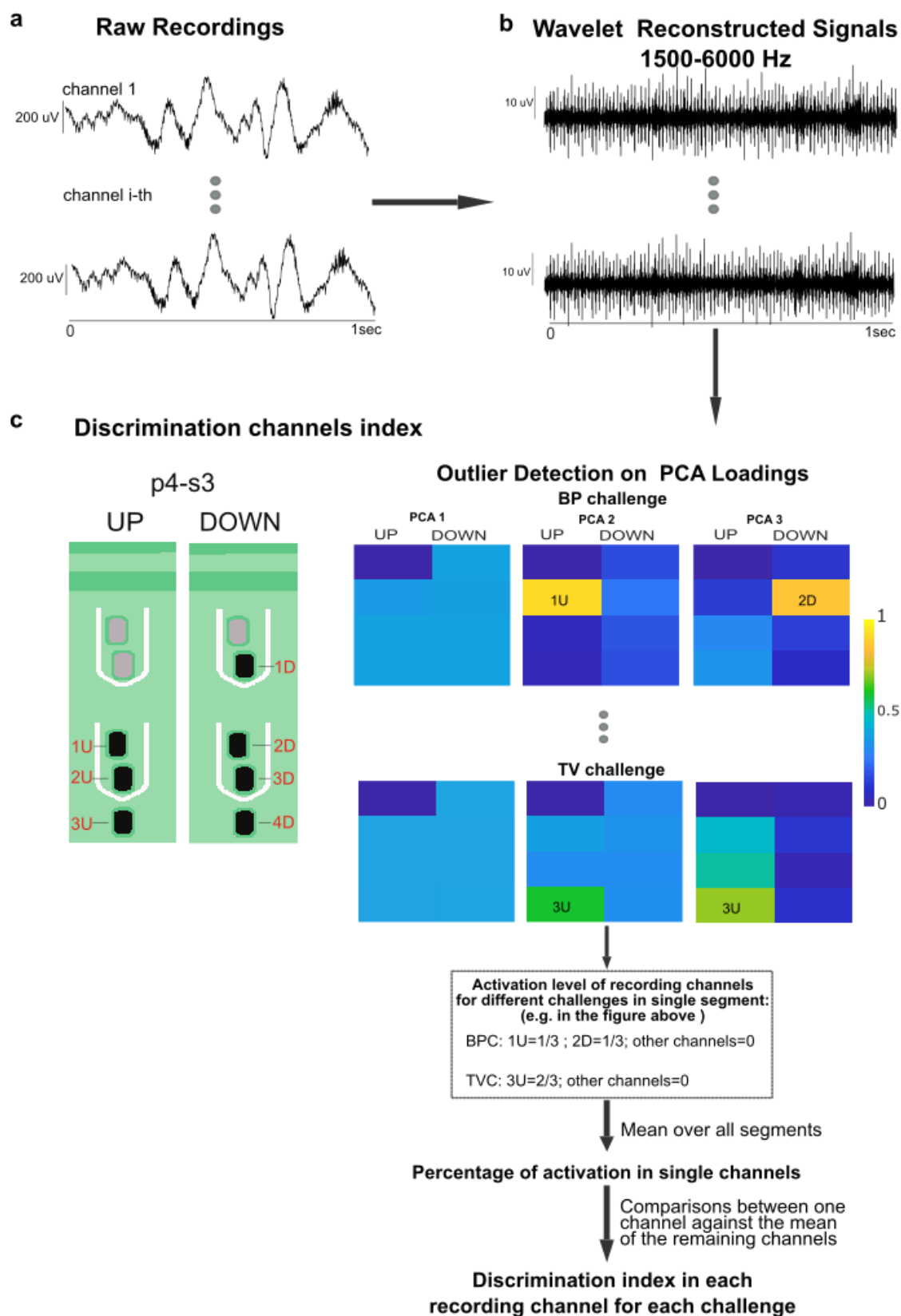
821 **Supplementary Figure 2**

Confusion Matrices Baseline vs. Two Challenges

822

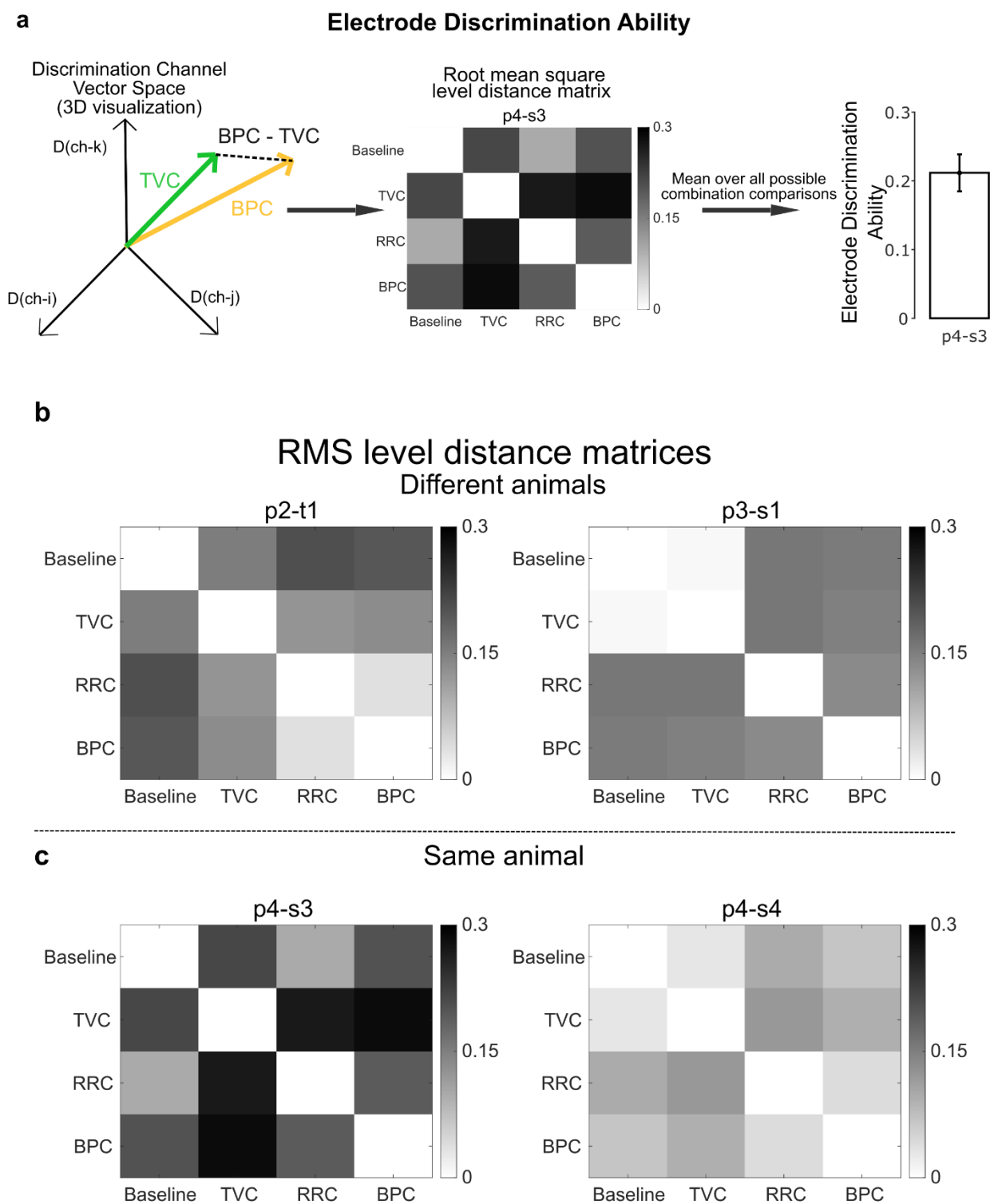823 **Supplementary Figure 3**

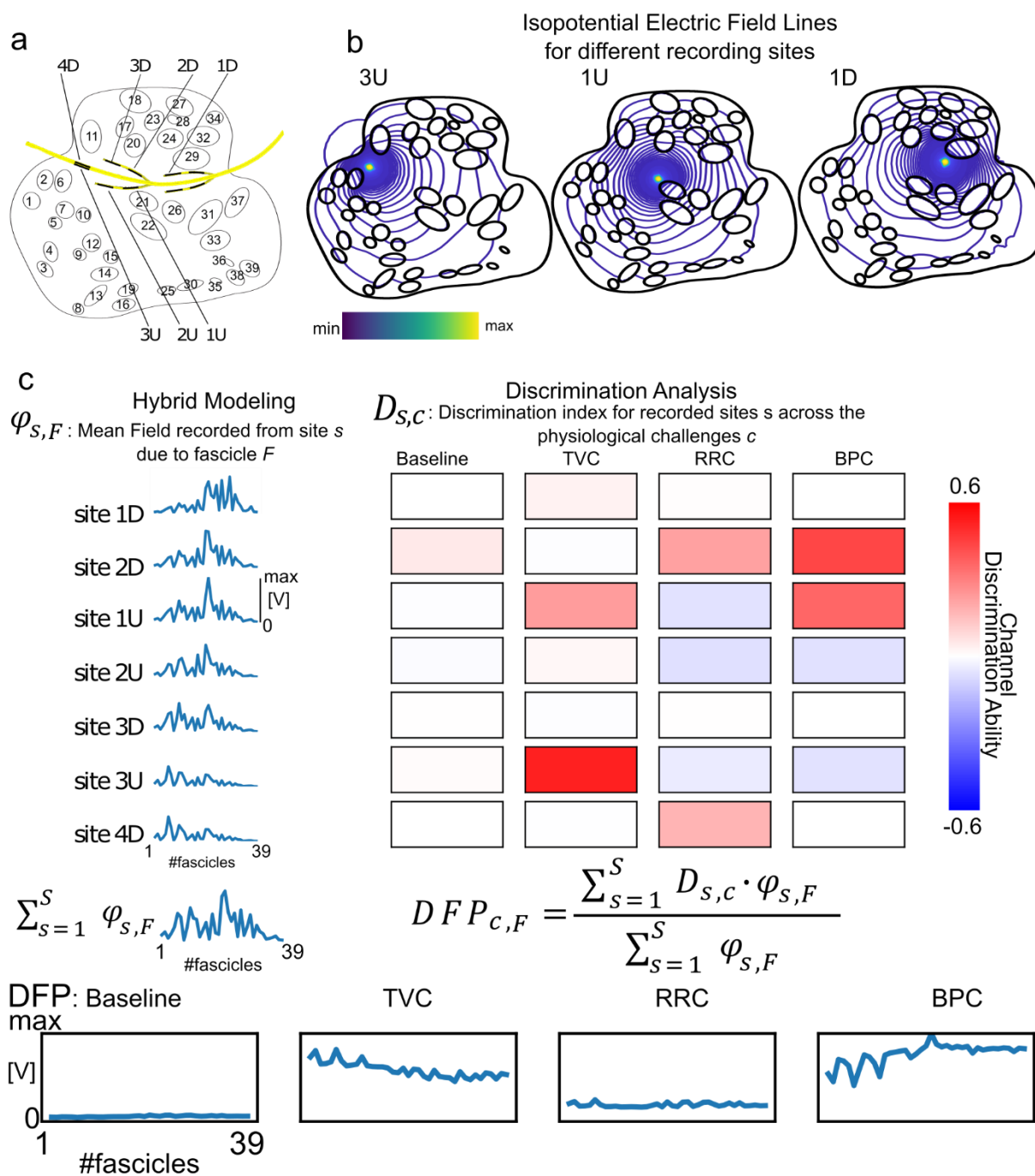

Discrimination Analysis Method

824

825

826 **Supplementary Figure 4**

a Electrode Discrimination Ability

b RMS level distance matrices
Different animals

c Same animal
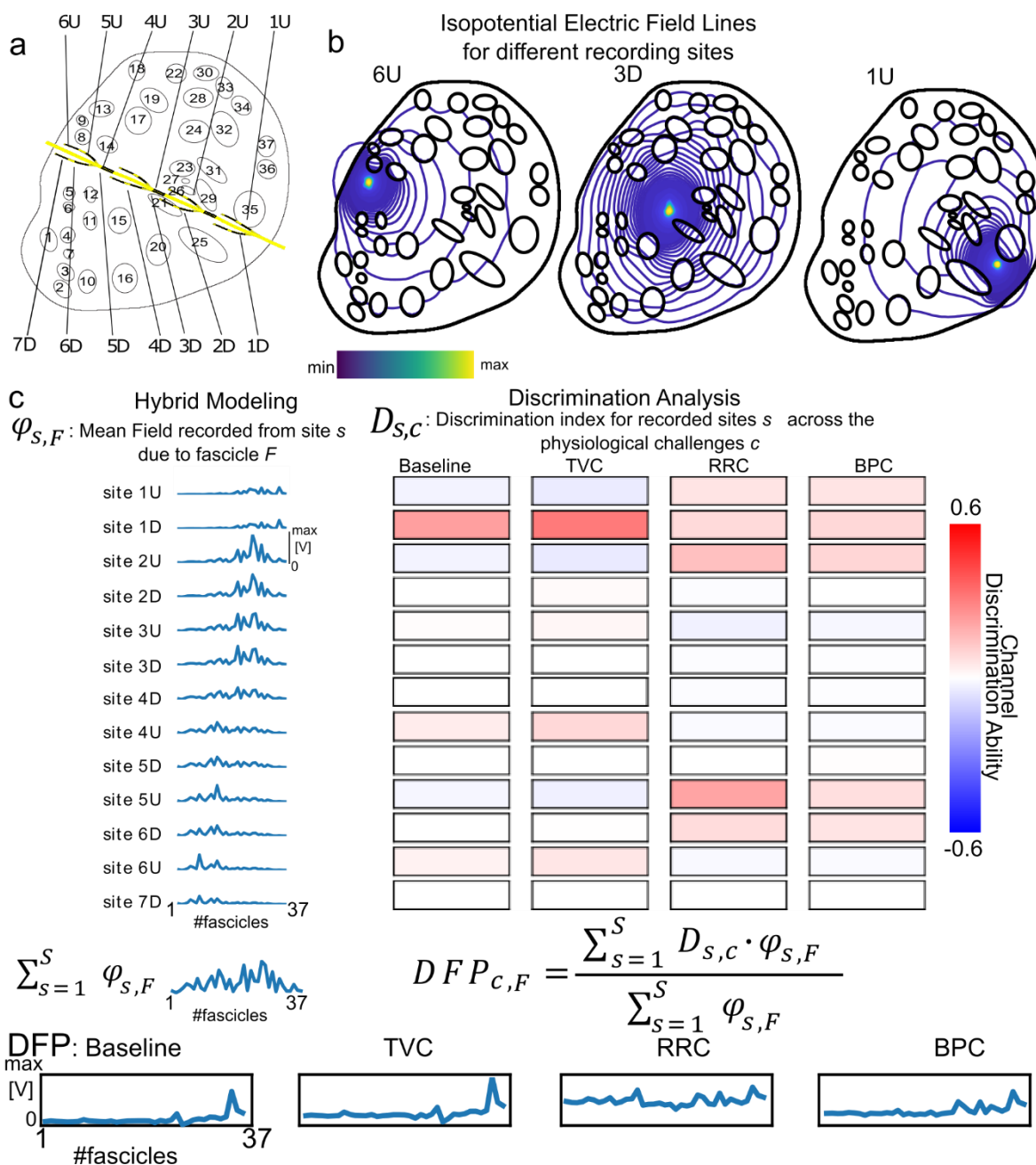
827

828 **Supplementary Figure 5**

829

830
831
832
833
834
835
836

837

838

839 **Supplementary Figure 6**

840

841